Nuclear Engineering and Technology 54 (2022) 1016–1023

Contents lists available at ScienceDirect

Nuclear Engineering and Technology

journal homepage: www.elsevier.com/locate/net

Original article

Upgrade of gamma electron vertex imaging system for high-performance range verification in pencil beam scanning proton therapy

Sung Hun Kim [a], Jong Hwi Jeong [a], Youngmo Ku [b], Jaerin Jung [b], Sungkoo Cho [c], Kwanghyun Jo [c], Chan Hyeong Kim [b, *]

[a] Center for Proton Therapy, National Cancer Center, Goyang-si, 10408, Gyeonggi-do, South Korea
[b] Department of Nuclear Engineering, Hanyang University, Seoul, 04763, South Korea
[c] Radiation Oncology, Samsung Medical Center, Seoul, 06351, South Korea

ARTICLE INFO

Article history:
Received 19 April 2021
Received in revised form
29 August 2021
Accepted 2 September 2021
Available online 8 September 2021

Keywords:
Prompt gamma imaging
Gamma electron vertex imaging
In-vivo range verification
Pencil beam scanning proton therapy
Proton therapy

ABSTRACT

In proton therapy, a highly conformal proton dose can be delivered to the tumor by means of the steep distal dose penumbra at the end of the beam range. The proton beam range, however, is highly sensitive to range uncertainty, which makes accurately locating the proton range in the patient difficult. *In-vivo* range verification is a method to manage range uncertainty, one of the promising techniques being prompt gamma imaging (PGI). In earlier studies, we proposed gamma electron vertex imaging (GEVI), and constructed a proof-of-principle system. The system successfully demonstrated the GEVI imaging principle for therapeutic proton pencil beams without scanning, but showed some limitations under clinical conditions, particularly for pencil beam scanning proton therapy. In the present study, we upgraded the GEVI system in several aspects and tested the performance improvements such as for range-shift verification in the context of line scanning proton treatment. Specifically, the system showed better performance in obtaining accurate prompt gamma (PG) distributions in the clinical environment. Furthermore, high shift-detection sensitivity and accuracy were shown under various range-shift conditions using line scanning proton beams.

1. Introduction

In proton therapy, proton beam produces a highly steep distal dose penumbra at the end of its range, thus enhancing tumor control probability while minimizing normal tissue complication probability. Proton therapy is considered a clinically superior treatment modality to conventional radiotherapies using photons and electrons [1–3]. The range of the proton beam is, however, very sensitive to several uncertainties such as patient-anatomical change between the fractions, patient setup error, computed tomography (CT) conversion error, and others [3–6], all of which make accurate prediction of the actual beam range in the patient very difficult. Due to these range uncertainties, radiation oncologist does not dare to locate the distal dose penumbra just in front of the organ at risk, consequently limiting the superiority of the proton's dosimetric characteristic. Instead, in current proton treatment practice, sub-optimal techniques are used: dose conformation based on lateral dose penumbra, safety margins, intensity-modulated proton therapy, etc. [1,3]. These alternative techniques, however, entail a delivery of a certain unwanted dose to adjacent normal tissues.

The above problem can be avoided by *in-vivo* range verification, and one of the most promising techniques is prompt gamma imaging (PGI). In PGI, the prompt gamma (PG) distribution has a strong correlation with the dose distribution, and moreover a real-time monitoring is possible because the PGs are generated within a few nano seconds after proton reactions with matter. Several PGI systems have been developed [7–11] since the first PGI's experimental demonstration in 2006 [12]. In this context, we proposed a new approach, called gamma electron vertex imaging (GEVI) [13]. In GEVI, as shown in Fig. 1, PGs are converted to electrons by Compton scatterings in an electron converter, and the Compton-recoiled electrons are traced with two hodoscopes and a

* Corresponding author. Department of Nuclear Engineering, Hanyang University, 222 Wangsimni-ro, Seongdong-gu, Seoul, 04763, South Korea.
E-mail address: chkim@hanyang.ac.kr (C.H. Kim).

https://doi.org/10.1016/j.net.2021.09.001

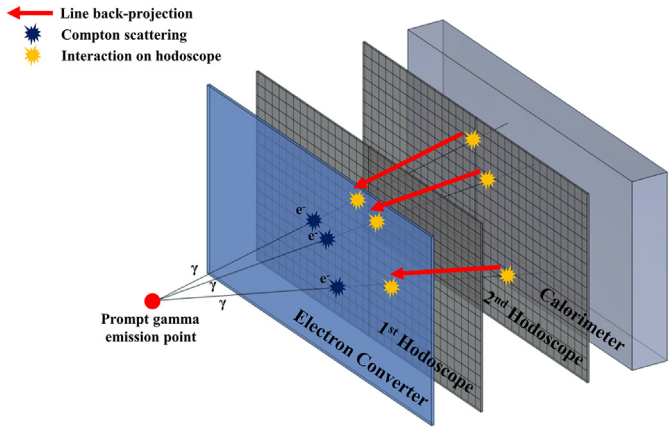

Fig. 1. Principle of gamma electron vertex imaging (GEVI).

calorimeter. The effective events are selected by triple coincidence and energy windows of the hodoscopes and the calorimeter. Using the interaction positions of the electrons, the PG emission points (i.e., PG vertices) are determined by simple back-projection method. The GEVI system has the following advantages over other collimation-based systems: (1) high sensitivity, (2) provision of two-dimensional images, and (3) significantly light weight (= ~0.75 kg for detectors).

In earlier studies, we constructed a proof-of-principle GEVI system [14,15] consisting of a beryllium plate, double-sided silicon strip detectors (DSSDs), and a plastic scintillation detector for the electron converter, the hodoscopes, and the calorimeter, respectively. The performance of the system was also evaluated for therapeutic proton pencil beams without scanning, and its imaging principle was successfully demonstrated: it was shown that the distal falloff region in a GEVI image is strongly correlated with the proton beam range [15]. The proof-of-principle system, however, had some limitations of its application in a clinical environment, especially for pencil beam scanning proton therapy. In pencil beam scanning proton therapy, the dose rate is very high therefore the detector signals cannot be processed properly thus locating the PG vertices inaccurately. Furthermore, the proton spots are scanned rapidly (within a few milliseconds for each spot), therefore the PG distributions for each spot cannot be acquired. In the present study, the GEVI system was upgraded in several aspects (i.e., system configuration, signal processing, and data acquisition (DAQ)), and its performance improvement was tested. Using the upgraded system, its performance for range-shift verification in line scanning proton therapy was also evaluated.

2. System upgrade

2.1. System configuration

Fig. 2 shows the configuration of the prototype GEVI system: isometric and top views are provided on the left and right sides of the figure, respectively. The component detectors of the prototype GEVI system remained the same as those of the proof-of-principle system. For the electron converter, a 200 (W) × 100 (H) × 10.8 (T) mm^3 beryllium plate of 99% purity was used. For each hodoscope, two DSSDs (W1 Type 9G, Micron Semiconductor Limited, UK) of 50 × 50 mm^2 detection area each were employed, thereby resulting in a 2 × 2 DSSD array and 100 × 50 mm^2 active areas. The thicknesses of the first and second hodoscopes were 150 μm and 300 μm, respectively. For the calorimeter, a plastic scintillation detector (Scionix Holland B.V., The Netherlands) was utilized, consisting of the EJ-200 plastic scintillator (Eljen Technology, USA) of 160 (W) × 85 (H) × 25 (T) mm^3 and a photomultiplier (R10601, Hamamatsu Photonics K.K., Japan) of 19 mm radius. The dedicated readout systems were employed for each component detector.

In the proof-of-principle system, however, the component detectors and the readout systems were not entirely enclosed with proper materials thereby not isolating them from outside world [16]. The previous system case could not fully protect the inside detectors and circuits from external electromagnetic interference. In the present study, therefore, we designed and constructed a new system case. This new system case was made of aluminum and entirely fenced the inside devices, thus properly shielding the electromagnetic interference.

2.2. Signal processing for hodoscopes

In signal processing for the hodoscopes, the GEVI system utilized a multiplexing system, which, however, had a long signal processing time of ~1.5 μs and prioritized the highest-order channel if more than two channels responded within the signal processing time. In the clinical dose rate, multiple channels usually respond during the signal processing time, thereby missing the PG-interacted channel and resulting in a low accuracy in the determination of PG vertices. Accordingly, we removed the multiplexing system from signal processing and utilized all channels of the

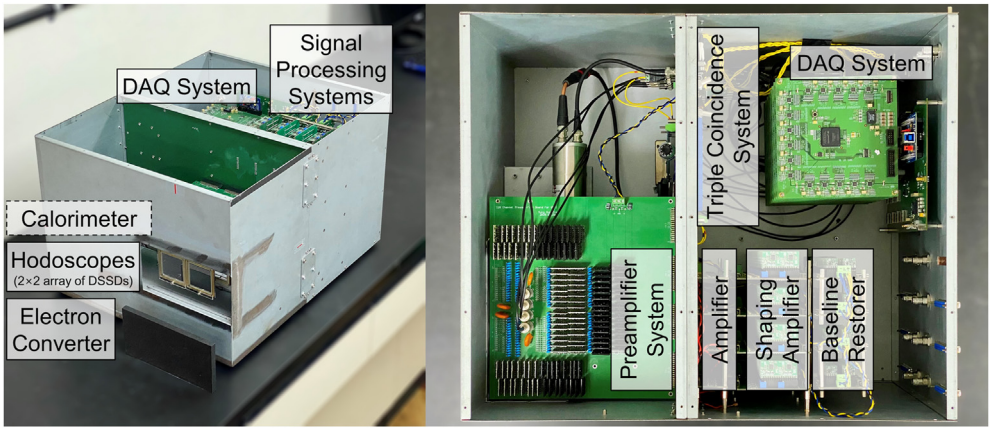

Fig. 2. Mechanical structure of prototype GEVI system in isometric (left) and top (right) views. In the isometric view, for better visualization of the inside of the structure, the beryllium electron converter is moved outside of its normal position, which is in front of the first hodoscope.

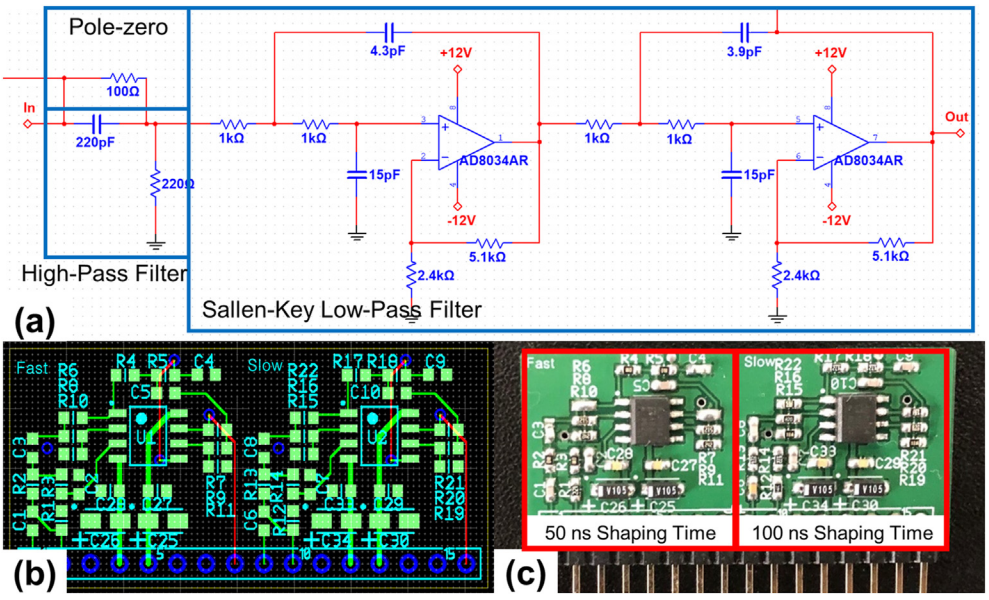

Fig. 3. Circuit diagram (a), layout design (b), and constructed printed circuit board (c) for developed shaping amplifier module. Two types of shaping amplifier with shaping times of 50 ns (for trigger logic generation) and 100 ns (for peak detection) were integrated into the module.

hodoscopes (i.e., 128 channels) to obtain GEVI images. In obtaining the GEVI image with the 128 channels, however, it was difficult to distinguish the effective PG vertex from the multiple responses, and consequently, the image quality was degraded. In the present study, therefore, the number of multiple interactions in the hodoscopes was reduced by optimizing the shaping time and the peak detection time. The shaping time is the time taken to render the hodoscope signal Gaussian-shaped, and the peak detection time is the time necessary to acquire the peak of the shaped signal for energy determination.

For the proof-of-principle system, the shaping times of 100 ns and 250 ns were applied, which were minimized to 50 ns and 100 ns according to the rising time of the DSSD. Note that the rising time of the DSSD was about 50 ns and that the shaping time cannot be shorter than the rising time. The 50 ns and 100 ns shaping times were utilized for trigger logic generation and energy determination, respectively. A new shaping amplifier module for the reduced shaping time was developed, as shown in Fig. 3. Fig. 3(a)–(b) show the circuit diagram and the layout for the amplifier module designed using Multisim and Ultiboard (National Instruments, USA), respectively. The CR differentiator and pole/zero correction were employed to reduce the decay time of the preamplifier signal and to minimize the under-/over-shoot of the output signal, respectively. An active filter with two Sallen-Key low-pass filters was utilized to generate the Gaussian-shaped output signal. The individual values of each resistor and capacitor were determined by trial and error. Fig. 3(c) shows the constructed printed circuit board.

The peak detection time was optimized for the appropriate energy determination using the 100 ns shaped signals, and the results are plotted in Fig. 4. In the optimization, the peak detection time was changed from 400 ns to 200 ns, because 400 ns corresponds to the width of the 100 ns shaped signal. The amplitude of the input signal was increased from 200 mV to 900 mV due to the 0–1,000 mV input range for the DAQ; otherwise, 100 mV signal could not be detected due to its being lower than the threshold level. Note that the normalized value of 1 on the y-axis indicates accurate peak detection. As a result, the optimal peak detection time was determined to be 325 ns, which was employed for the DAQ system, as will be discussed later.

For further improvement of signal processing for hodoscopes, a systematic noise of the preamplifier system was reduced. The measurement of PG distribution was disturbed by the systematic noise, thus deteriorating the imaging efficiency and the imaging quality. The main source of the noise was a weak-to-noise design of the preamplifier system. Typically, the detectors and the preamplifiers should be positioned as close as possible to reduce noise, because signals initially generated from the detector are highly prone to contamination by various source of noise; that is, stable transmission of detector signals is very important. In the proof-of-principle GEVI system, however, the preamplifiers were not located close to the DSSDs, and the DSSD signals were transmitted through the non-coaxial flat cables, which are very weak to noise. In the present study, therefore, the preamplifier system was redesigned and constructed. The DSSDs were directly installed on the new preamplifier system not using any cables. Furthermore, the preamplifier chips were positioned very close to the DSSDs.

2.3. Data acquisition

Pencil beam scanning proton therapy consists of numerous energy layers and spots, and the proton beam for each spot is scanned very quickly. Therefore, the PG distribution for each spot should be obtained automatically at high speed. In this context, a high-speed DAQ system, which can automatically acquire the PG data for each spot, was developed. The new DAQ system was based on a high performance FPGA (field programmable gate array) and utilized beam-on signals from cyclotron, each beam-on signal indicating the state of the beam irradiation for individual spots. Acquiring data is triggered by these beam-on signals thereby obtaining the PG distributions for each spot automatically. Due to the numerous channels of the GEVI system (i.e., 128 channels of the DSSDs and 1 channel of the plastic scintillation detector), the DAQ system consists of 8 slave modules and a master module. The slave modules measure the signals of the DSSDs. The master module measures the signal of the plastic scintillation detector and merges the acquired data from all modules. Then the integrated PG data is transferred to a personal computer using a USB controller. For the master module, an FPGA (5CEBA7F31C7N, Altera, USA), an ADC

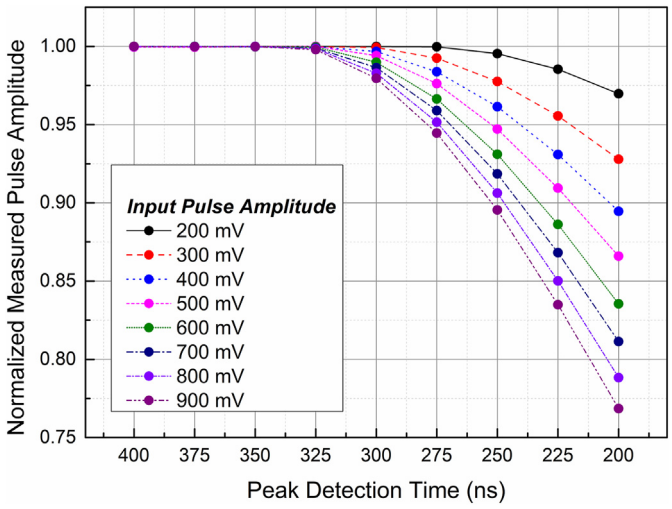

Fig. 4. Distribution of measured peak amplitude for different peak detection times and input pulse amplitudes. The measured peak amplitudes were normalized with the original amplitude (i.e., input amplitude). Note that the normalized value of 1 on the y-axis indicates accurate peak detection.

(analog-to-digital converter; AD9245, Analog Devices, Inc., USA) and a USB controller (CYUSB3KIT-003, Cypress, USA) were utilized. For the slave modules, an FPGA (EP3C40F484C8N, Altera, USA) and ADCs were employed.

3. Experiment and data analysis methods

3.1. Experiment using single proton pencil beam

The performance improvement from the system upgrade was evaluated in terms of the number of multiple interactions in the hodoscopes, the proportion of true PG vertices, and the imaging efficiencies. The number of multiple interactions in the hodoscopes and the proportion of true PG vertices were estimated for both simulations and experiments, because multiple responses cannot be detected experimentally using the proof-of-principle GEVI system. Note that the multiplexing system in the proof-of-principle system had the priority to take only the highest-order channel, if more than two channels responded within the signal processing time. On the other hand, the imaging efficiency was estimated for experiments only, because the effects on imaging efficiency by upgrading the signal processing for the hodoscopes and the DAQ cannot be fully considered in simulations.

Firstly, for the simulation, Geant4 Monte Carlo simulation toolkit (ver. 10.04.p02) [17] was utilized. The proton beams of 90, 120, 150, and 180 MeV were irradiated to a homogeneous PMMA (polymethyl methacrylate, density = 1.18 g/cm^3) slab phantom of 300 × 300 × 300 mm^3. The center of the GEVI system was focused on at each proton beam range. The distance between the GEVI system and the beam axis was 70 mm. The number of delivered protons was 10^9. The interaction time of the component detectors was recorded in consideration of the microbunch time structure of the proton pencil beam and the timing resolutions of the detectors. The modular physics list QGSP_BERT_HP was employed to simulate the particle interactions.

Secondly, for the experiment, the therapeutic proton beam at Samsung Medical Center (SMC) in Korea was utilized. The proton pencil beam, extracted from the 230 MeV cyclotron (Sumitomo Corp., Japan), was irradiated and the generated PGs were measured by the GEVI system. The experimental conditions, including phantom, beam energy, and system position, were same as in the simulation. The number of delivered protons was 6.24×10^9.

3.2. Experiment using line scanning proton beam

The performance of the GEVI system for range-shift verification was evaluated using therapeutic line scanning proton beams at SMC. The planning target volumes (PTVs) of spherical and cubic shapes were defined in the homogeneous PMMA slab phantom of 300 × 300 × 300 mm^3: 382 mm^3 and 512 cm^3 volumes for the spherical and cubic PTVs, respectively. The prescribed dose was 60 Gy, assuming a constant relative biological effectiveness (RBE) of 1.1 with 30 fractions and two equally weighted fields, thereby resulting in 1 Gy/field. Six consecutive energy layers (from the second to the seventh) in one of the two fields (270° gantry angle) were monitored. Close-to-clinical range-shift scenarios were introduced on the assumption of anatomical change in the patient; accordingly, additional PMMA plates for range shifting were located on the beam path. For global shift, the plate covered the complete beam exit, and for local shift, half of the snout was blocked by the plates. The magnitudes of the shifts were 0, 1, 2, 4, and 8 mm for each range-shift scenario. The 0 mm range-shift scenario was considered as no shift case. The center of the GEVI system was fixed at the isocenter, and the distance between the system and the isocenter was 80 mm. A relative change of centroid in the PG distribution was converted to a relative change of beam range (i.e., range shift).

3.3. Data analysis for segmentation of line scanning proton beam

The line scanning proton treatment comprises numerous line segments (i.e., basic beam irradiation units), and the proton beams are irradiated by continuous scanning for each energy layer while the scanning speed is modulated at a constant dose rate. Due to the continuous beam scanning, the PG distributions for each whole energy layer are obtained, which requires segmentation of the PG distribution for the individual line segments. In the present study, a method for segmentation of line scanning proton beams was applied, according to which the integrated PG distribution for each energy layer is measured in chronological order and then divided in correspondence to the beam scanning times for each line segment. The beam scanning time was calculated based on the length and scanning speed of the line segment.

3.4. Data analysis for spot aggregation

In pencil beam scanning proton therapy, the PG distributions are highly sensitive to Poisson noise due mainly to the low PG statistics. Better range-shift verification can be performed with lower Poisson noise, and reduced noise can be obtained with a greater number of delivered protons. In the present study, spot aggregation was employed to overcome the low PG statistics where the PG distributions for neighboring spots are clustered, each spot being replaced by the summation of the weighted neighboring spots [9]. The weights were calculated in consideration of the Gaussian probability density function (sigma = 8.0 mm) and the proton numbers for each spot.

4. Results and discussion

4.1. Performance improvements

The results for the performance improvements of the GEVI system are displayed in Table 1. First, the number of multiple interactions in the hodoscopes, which is an important parameter for accurate determination of the PG vertices on a GEVI image, was

Table 1
Performances of proof-of-principle GEVI system and prototype GEVI system in terms of number of multiple interactions in hodoscopes, proportion of true prompt gamma vertices, imaging efficiency in FOV, and imaging efficiency in ROI.

Number of Multiple Interactions in Hodoscopes			
	Proof-of-principle System	**Prototype System**	
	Simulation	Simulation	Experiment
1st Hodoscope	2.37	1.37	1.61
2nd Hodoscope	2.11	1.26	1.46

Proportion of True Prompt Gamma Vertices		
Proof-of-principle System	**Prototype System**	
Simulation	Simulation	Experiment
20%	58%	43%

Imaging Efficiency in FOV	
Proof-of-principle System	**Prototype System**
Experiment	Experiment
1.30×10^{-6}	1.85×10^{-6}

Imaging Efficiency in ROI (within 3σ of beam position uncertainty)	
Proof-of-principle System	**Prototype System**
Experiment	Experiment
5.11×10^{-7}	1.13×10^{-6}

evaluated. Note that because the proof-of-principle system cannot record multiple responses, only the simulation result was evaluated. As shown in Table 1, the prototype showed only about half of the multiple interactions in the proof-of-principle system, and a greater decrease for the first hodoscope was found due to the higher count rate than in the case of the second hodoscope. The experimental results showed more responses than the simulation, owing to the absence of any modeling of the beam nozzle or other geometries in the simulation.

Second, the proportion of true PG vertices was 20% for the proof-of-principle system, whereas it was highly increased to 58% for the prototype system. This result reflects the enhanced accuracy of the GEVI system for determination of PG vertices. The experimentally evaluated proportion was lower than the simulation result, due to the reason aforementioned: that is, the discrepancy between the experiments and the simulations.

Third, two types of imaging efficiency were evaluated: field of view (FOV) and region of interest (ROI). The FOV imaging efficiency was calculated as the number of effective vertices in the entire FOV divided by the number of delivered protons; the ROI imaging efficiency, however, was calculated according to only the vertices within the position uncertainty of the proton beam, which are practically helpful for beam-range verification. The position uncertainty (1σ) of the therapeutic proton beam was varied from ~3 mm to ~10 mm for 180 MeV down to 90 MeV. The 3σ position uncertainty was applied to account for the beam positions within the 99.7% confidence interval. As a result, the FOV and ROI imaging efficiencies were increased 1.4 and 2.2 times, respectively. The better improvement for ROI was owed to the fact that a greater number of PG vertices were determined within the region near the beam axis.

4.2. Range-shift verification

Fig. 5 shows the representative results of range-shift map for the third energy layer of each PTV. On the range-shift maps, the estimated range shifts are plotted at each position of the line segments in the beam's eye view (BEV). The amount of range shift is represented with the colors based on the scale on the right side of the figure. For the local shift scenarios, the vertical lines indicate the boundaries of local shift; the left side of the boundary is the shifted area. The layer-averaged shift with the standard deviation (1σ) is given at the bottom of each map. As presented in Fig. 5, the measured range shifts showed a clear tendency according to shift scenario. The colors were blue and red for the negative and positive shifts, respectively, and became darker for a large amount of shift. The layer-averaged global shifts, including no shift, well agreed with the introduced shift values; however, the layer-averaged local shifts were altered due to the range mixing effect. In certain regions, low accuracy of shift estimation was found, especially at the left corners where the PG distributions still suffered from insufficient PG statistics due to geometrical factors: the smaller number of protons than at the center of the layer after spot aggregation, and the longer distance from the GEVI system. Note that the GEVI system measured the PG distributions on the right side of the layers in the BEV, and that therefore, higher imaging efficiency was obtained on the right side. These fluctuations nevertheless did not affect the overall range-shift verification results.

Fig. 6(a)–(b) represent the 99% confidence intervals of the estimated range shifts for each PTV along with the results of the statistical hypothesis tests performed using IBM SPSS Statistics 26 (IBM, Armond, USA) with the 5% significance level: one-sample t-tests and one-way analysis of variances (ANOVAs) as black and gray asterisks, respectively. These asterisks for each hypothesis test

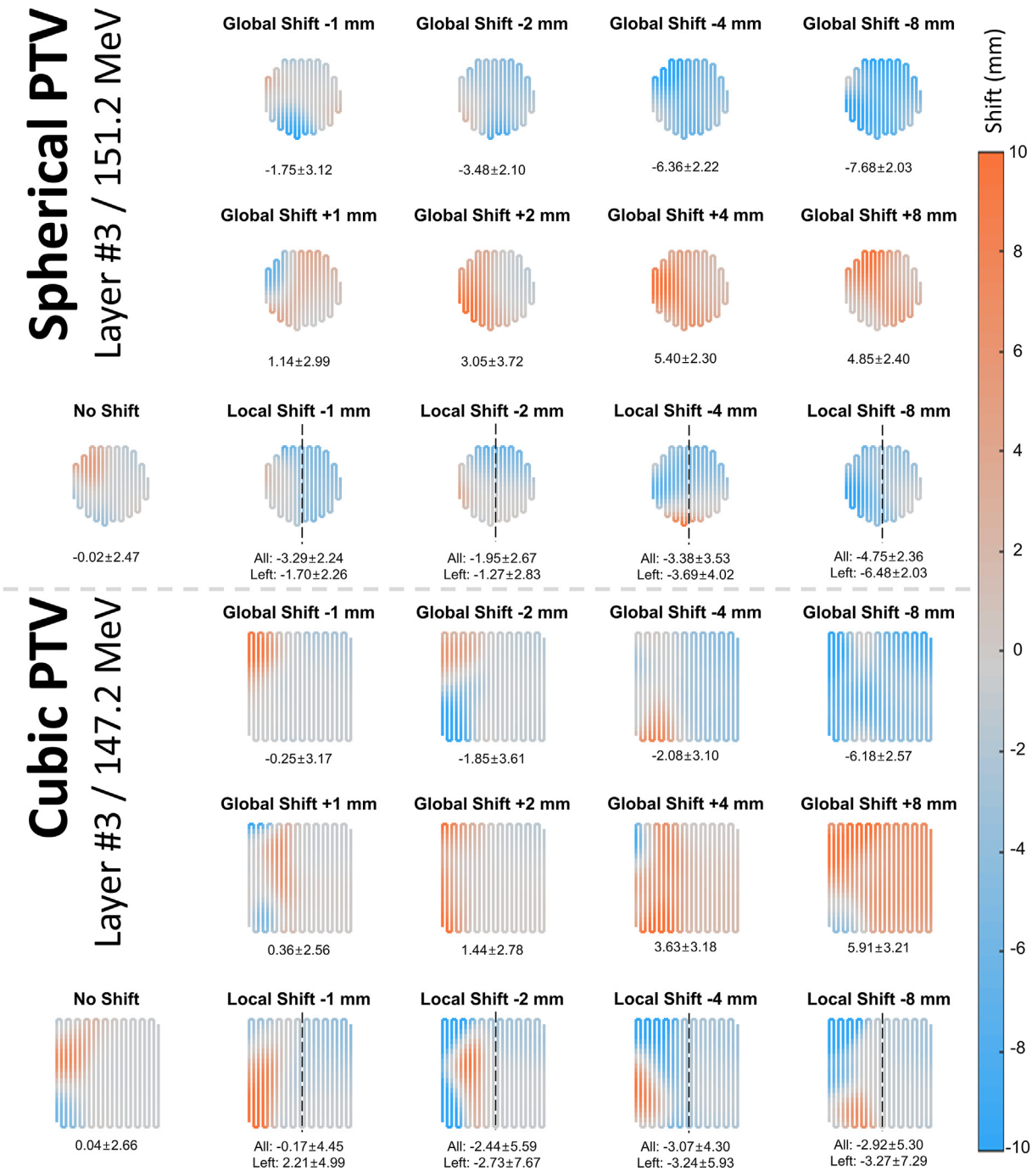

Fig. 5. Range-shift map in beam's eye view (BEV) of spherical (upper) and cubic (lower) planning target volumes (PTVs) in slab phantom for third distal energy layer as representative cases. The spot sizes are proportional to the number of protons. The vertical lines indicate the boundary of local shift, the left side of the boundary being the shifted area. The layer-averaged shift with the standard deviation (1σ) is given at the bottom of each map.

indicate significant difference of measured shift from zero and from one another, respectively. The confidence intervals and the statistical hypothesis tests were evaluated using the data for all energy layers. As shown in Fig. 6, the no shift cases were not significantly different from zero. Whereas, for the global shifts, the introduced shifts were clearly observable. The measured shifts differed significantly from zero and agreed with the expectation to an accuracy of 0.4 mm. The difference between individual global shifts was also statistically significant. The evaluation of local shifts showed a rather low accuracy of 1.9 mm, underestimating the negative shifts in general. This underestimation resulted from range mixing near the shift boundary following spot aggregation. Low PG statistics, especially in the proximal layers, resulted in a high level of Poisson noise, and there was a larger impact for some small local shifts (i.e., −1 mm and −2 mm for the spherical and cubic PTVs, respectively), which overestimated the shifts. Nevertheless, all of the measured local shifts showed significant differences from zero.

Table 2 shows a confusion matrix for range-shift determination of both spherical and cubic PTVs. The confusion matrix was based

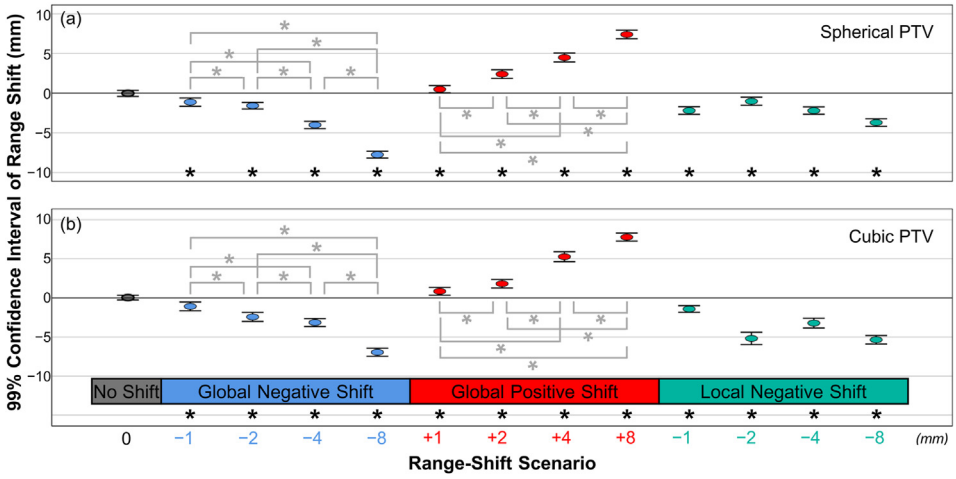

Fig. 6. 99% confidence intervals of estimated range shifts for (a) spherical and (b) cubic planning target volumes (PTVs) along with statistical hypothesis test results with 5% significance level: one-sample t-tests and one-way analysis of variances (ANOVAs) in black and gray asterisks, respectively. The asterisks for each hypothesis test indicate significant difference of measured shift from zero and from one another, respectively.

Table 2
Confusion matrix for range-shift determination of both spherical and cubic PTVs. The confusion matrix was based on the results of one-sample t-tests using the layer-averaged shift data.

Spherical and Cubic PTV		Detected Shift	
		Yes	No
Actual Shift	Yes	117	27
	No	2	10

on the results of one-sample t-tests using the data of each energy layer. As presented in Table 2, the true positive/negative rates were 81.3% and 83.3%, respectively; which means that the range-shift verification by using the GEVI system would be correct with 81.4% average reliability. These rates, however, were increased if the range-shift determination is performed based on the data of all energy layer. Note that the true positive/negative rates are 100% as shown in Fig. 6.

5. Conclusion

In the present study, the GEVI system was upgraded to overcome some limitations of its application to pencil beam scanning proton therapy, specifically by enhancing the system configuration, the signal processing for the hodoscopes, and the DAQ. The consequent performance improvement was evaluated for both the experiments using single proton pencil beams at SMC and Geant4 Monte Carlo simulations. The upgraded system showed better results in achieving more accurate PG distributions in the clinical environment on account of the reduced number of interactions in the hodoscopes, the increased proportion of true PG vertices, and the higher imaging efficiency. Furthermore, the performance of range-shift verification in pencil beam scanning proton therapy was estimated for the various conditions of range-shift scenarios using the line scanning proton beams at SMC. Our results showed high shift-detection sensitivity: down to 1 mm shifts were perceived for both global and local shifts. High shift-detection accuracy was also shown in the determination of global and local shifts within 0.4 mm and 1.9 mm error, respectively. In the near future, the system performance for range-shift verification in spot scanning proton treatment will be evaluated under more-various conditions.

Declaration of competing interest

The authors declare that they have no known competing financial interests or personal relationships that could have appeared to influence the work reported in this paper.

Acknowledgements

This research was supported by the National Cancer Center Grants (NCC-2110390-1), Korea.

References

[1] A.C. Knopf, A. Lomax, In vivo proton range verification: a review, Phys. Med. Biol. 58 (15) (2013) R131, https://doi.org/10.1088/0031-9155/58/15/R131.
[2] J. Krimmer, D. Dauvergne, J.M. Létang, Testa, Prompt-gamma monitoring in hadrontherapy: a review, Nucl. Instruments Methods Phys. Res. Sect. A Accel. Spectrometers, Detect. Assoc. Equip. 878 (2018) 58–73, https://doi.org/10.1016/j.nima.2017.07.063.
[3] H. Paganetti, Range uncertainties in proton therapy and the role of Monte Carlo simulations, Phys. Med. Biol. 57 (2012) R99, https://doi.org/10.1088/0031-9155/57/11/R99.
[4] G. Pausch, J. Berthold, W. Enghardt, K. Römer, A. Straessner, A. Wagner, T. Werner, T. Kögler, Detection systems for range monitoring in proton therapy: needs and challenges, Nucl. Instruments Methods Phys. Res. Sect. A Accel. Spectrometers, Detect. Assoc. Equip. 954 (2020) 161227, https://doi.org/10.1016/j.nima.2018.09.062.
[5] I. Perali, A. Celani, P. Busca, C. Fiorini, A. Marone, M. Basilavecchia, T. Frizzi, F. Roellinghoff, J. Smeets, D. Prieels, F. Stichelbaut, F. Vander Stappen, S. Henrotin, A. Benilov, Prompt gamma imaging with a slit camera for real-time range control in proton therapy: experimental validation up to 230 MeV with HICAM and development of a new prototype, in: IEEE Nuclear Science Symposium and Medical Imaging Conference Record, 2012, pp. 3883–3886, https://doi.org/10.1109/NSSMIC.2012.6551890. NSS/MIC.
[6] J. Smeets, F. Roellinghoff, D. Prieels, F. Stichelbaut, A. Benilov, P. Busca, C. Fiorini, R. Peloso, M. Basilavecchia, T. Frizzi, J.C. Dehaes, A. Dubus, Prompt gamma imaging with a slit camera for real-time range control in proton therapy, Phys. Med. Biol. 57 (11) (2012) 3371–3405, https://doi.org/10.1088/0031-9155/57/11/3371.
[7] C.H. Min, H.R. Lee, C.H. Kim, S.B. Lee, Development of array-type prompt gamma measurement system for in vivo range verification in proton therapy, Med. Phys. 39 (4) (2012) 2100–2107, https://doi.org/10.1118/1.3694098.
[8] J. Krimmer, M. Chevallier, J. Constanzo, D. Dauvergne, M. De Rydt, G. Dedes, N. Freud, P. Henriquet, C. La Tessa, J.M. Létang, R. Pleskac, M. Pinto, C. Ray, V. Reithinger, M.H. Richard, I. Rinaldi, F. Roellinghoff, C. Schuy, E. Testa, M. Testa, Collimated prompt gamma TOF measurements with multi-slit multi-detector configurations, J. Instrum. 10 (2015) P01011, https://doi.org/10.1088/1748-0221/10/01/P01011, 01.
[9] Y. Xie, E.H. Bentefour, G. Janssens, J. Smeets, F. Vander Stappen, L. Hotoiu, L. Yin, D. Dolney, S. Avery, F. O'Grady, D. Prieels, J. McDonough, T.D. Solberg, R.A. Lustig, A. Lin, B.K.K. Teo, Prompt gamma imaging for in vivo range verification of pencil beam scanning proton therapy, Int. J. Radiat. Oncol. Biol.

Phys. 99 (1) (2017) 210–218, https://doi.org/10.1016/j.ijrobp.2017.04.027.
[10] S.W. Peterson, D. Robertson, J. Polf, Optimizing a three-stage Compton camera for measuring prompt gamma rays emitted during proton radiotherapy, Phys. Med. Biol. 55 (22) (2010) 6841–6856, https://doi.org/10.1088/0031-9155/55/22/015.
[11] C.H. Min, H.R. Lee, C.H. Kim, Two-dimensional prompt gamma measurement simulation for in vivo dose verification in proton therapy: a Monte Carlo study, Nucl. Technol. 175 (1) (2011) 11–15, https://doi.org/10.13182/NT11-A12262.
[12] C.H. Min, C.H. Kim, M.Y. Youn, J.W. Kim, Prompt gamma measurements for locating the dose falloff region in the proton therapy, Appl. Phys. Lett. 89 (18) (2006) 183517, https://doi.org/10.1063/1.2378561.
[13] C.H. Kim, J.H. Park, H. Seo, H.R. Lee, Gamma electron vertex imaging and application to beam range verification in proton therapy, Med. Phys. 39 (2) (2012) 1001–1005, https://doi.org/10.1118/1.3662890.
[14] H.R. Lee, S.H. Kim, J.H. Park, W.G. Jung, H. Lim, C.H. Kim, Prototype system for proton beam range measurement based on gamma electron vertex imaging, Nucl. Instruments Methods Phys. Res. Sect. A Accel. Spectrometers, Detect. Assoc. Equip. 857 (2017) 82–97, https://doi.org/10.1016/j.nima.2017.03.022.
[15] C.H. Kim, H.R. Lee, S.H. Kim, J.H. Park, S. Cho, W.G. Jung, Gamma electron vertex imaging for in-vivo beam-range measurement in proton therapy: experimental results, Appl, Phys. Lett. 113 (11) (2018) 114101, https://doi.org/10.1063/1.5039448.
[16] Nakhostin Mohammad, Signal Processing for Radiation Detectors, 2017. John Wiley & Sons.
[17] J. Allison, K. Amako, J. Apostolakis, P. Arce, M. Asai, T. Aso, E. Bagli, A. Bagulya, S. Banerjee, G. Barrand, B.R. Beck, A.G. Bogdanov, D. Brandt, J.M.C. Brown, H. Burkhardt, P. Canal, D. Cano-Ott, S. Chauvie, K. Cho, G.A.P. Cirrone, G. Cooperman, M.A. Cortés-Giraldo, G. Cosmo, G. Cuttone, G. Depaola, L. Desorgher, X. Dong, A. Dotti, V.D. Elvira, G. Folger, Z. Francis, A. Galoyan, L. Garnier, M. Gayer, K.L. Genser, V.M. Grichine, S. Guatelli, P. Guèye, P. Gumplinger, A.S. Howard, I. Hřivnáčová, S. Hwang, S. Incerti, A. Ivanchenko, V.N. Ivanchenko, F.W. Jones, S.Y. Jun, P. Kaitaniemi, N. Karakatsanis, M. Karamitrosi, M. Kelsey, A. Kimura, T. Koi, H. Kurashige, A. Lechner, S.B. Lee, F. Longo, M. Maire, D. Mancusi, A. Mantero, E. Mendoza, B. Morgan, K. Murakami, T. Nikitina, L. Pandola, P. Paprocki, J. Perl, I. Petrović, M.G. Pia, W. Pokorski, J.M. Quesada, M. Raine, M.A. Reis, A. Ribon, A. Ristić Fira, F. Romano, G. Russo, G. Santin, T. Sasaki, D. Sawkey, J.I. Shin, I.I. Strakovsky, A. Taborda, S. Tanaka, B. Tomé, T. Toshito, H.N. Tran, P.R. Truscott, L. Urban, V. Uzhinsky, J.M. Verbeke, M. Verderi, B.L. Wendt, H. Wenzel, D.H. Wright, D.M. Wright, T. Yamashita, J. Yarba, H. Yoshida, Recent developments in GEANT4, Nucl. Instruments Methods Phys. Res. Sect. A Accel. Spectrometers, Detect. Assoc. Equip. 835 (1) (2016) 186–225, https://doi.org/10.1016/j.nima.2016.06.125.